Crystallization

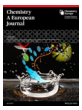

Synthesis and Assembly of Zinc Oxide Microcrystals by a Low-Temperature Dissolution–Reprecipitation Process: Lessons Learned About Twin Formation in Heterogeneous Reactions

Rudolf C. Hoffmann,[a] Maximilian Trapp,[b] Emre Erdem,[c] Markus Kratzer,[d] Christian Teichert,[d] Hans-Joachim Kleebe,[b] and Jörg J. Schneider*[a]

Dedicated to Prof. Dr. mult. Manfred Scheer on the occasion of his 65th birthday

Abstract: Cobalt-doped zinc oxide single crystals with the shape of hexagonal platelets were synthesized by thermohydrolysis of zinc acetate, cobalt acetate, and hexamethylenetetramine (HMTA) in mixtures of ethanol and water. The mineralization proceeds by a low-temperature dissolution–reprecipitation process from the liquid phase by the formation of basic cobalt zinc salts as intermediates. The crystal shape as well as twin formation of the resulting oxide phase can be influenced by careful choice of the solvent mixture and the amount of doping. An understanding of the course of the reaction was achieved by comprehensive employment of analytical techniques (i.e., SEM, XRD, IR) including an in-depth HRTEM study of precipitates from various reaction stages. In addition, EPR as well as UV/Vis spectroscopic measurements provide information about the insertion of the cobalt dopant into the zincite lattice. The Langmuir–Blodgett (LB) technique is shown to be suitable for depositing coatings of the platelets on glass substrates functionalized with polyelectrolyte multilayers and hence is applied for the formation of monolayers containing domains with ordered tessellation. No major differences are found between deposits on substrates with anionic or cationic surface modification. The adherence to the substrates is sufficient to determine the absolute orientation of the deposited polar single crystals by piezoresponse force microscopy (PFM) and Kelvin probe force microscopy (KPFM) studies.

1. Introduction

The morphology of inorganic micro-/nano-scale materials is one of the essential factors determining the functional properties that strongly depend on shape and size. Therefore, it is necessary to understand the underlying mechanisms for particle formation on the smallest utmost size.[1] Rational control over the synthesis of micro-/nano-scale structures has thus been a long-standing goal in the development of bottom-up device fabrication processes.[2] Zinc oxide is known to exist in a wide variety of different particle sizes and shapes when formed from solution, and it exhibits a plethora of morphologies ranging from simple geometries to complex, often polycrystalline arrangements.[3,4] In particular, 2D ZnO structures (sometimes denoted as plates, sheets or discs) have attracted wide attention due to their promising potential in many areas ranging from catalysis to electronics and chemical sensing.[5] The manufacturing of well-defined and equally sized hexagonal platelets in the micrometer regime would provide access to bottom-up techniques, which could allow for the fabrication of new devices, for example. The inherent ability for the self-assembly of objects such as equally sized hexagons was demonstrated by employing metal plates (approximately 10 μm) that were oriented by capillary forces, leading to the formation of ordered arrays and stacks.[6,7] In another example, uniform hexagonal platelets of cobalt hydroxide were synthesized by a

[a] Dr. R. C. Hoffmann, Prof. Dr. J. J. Schneider
Eduard-Zintl-Institut für Anorganische und Physikalische Chemie
Technische Universität Darmstadt
Alarich-Weiss-Strasse 12
64287 Darmstadt (Germany)
E-mail: joerg.schneider@ac.chemie.tu-darmstadt.de

[b] M. Trapp, Prof. Dr. H.-J. Kleebe
Institut für Angewandte Geowissenschaften
Technische Universität Darmstadt
Schnittspahnstrasse 9
64287 Darmstadt (Germany)

[c] Dr. E. Erdem
Materials Science and Nanoengineering
Sabanci University
34956, Tuzla İstanbul (Turkey)

[d] Dr. M. Kratzer, Prof. Dr. C. Teichert
Institut für Physik
Montanuniversität Leoben
Franz-Josef-Strasse 18
8700 Leoben (Austria)

Supporting information and the ORCID identification number(s) for the author(s) of this article can be found under: https://doi.org/10.1002/chem.201904638.

Part of a Special Issue on Low Temperature Solution Route Approaches to Oxide Functional Nanoscale Materials.

chemical bath process. The alignment of the ceramic disks with a size of about 2 μm and a thickness of about 100 nm was achieved by the Langmuir–Blodgett (LB) technique. These films were converted to cobalt oxide afterwards and successfully integrated in a sensor device.[8]

Surprisingly, for zinc oxide, no satisfactory route is currently available for the synthesis of single-crystalline hexagonal platelets. Several studies on the thermohydrolysis of various zinc salts report the synthesis of zinc oxide in the form of platelets.[9–16] The formation of well-defined and uniform single crystals is, however, rarely observed and the quantitative yield is described to be rather low.[9,10] Most of these procedures suffer from the heterogeneity of the obtained product.[11] Furthermore, organic surfactants[12] are difficult to remove after the initial formation of the oxide, and the strongly coordinating anions[13,14] might lead to the formation of basic zinc salts. Even the addition of metallic zinc as a template for heterogeneous nucleation was proposed.[15,16] The best control over the crystallization process (and thus the formation of well-defined crystals) can be achieved by the employment of strongly coordinating anions (citrate[17] or acetate[18]), the choice of solvent (*N*,*N*-dimethylformamide[19] or ethanol/water mixtures[10,20]), as well as doping with cobalt or magnesium.[21] Although the influence of these reaction parameters as growth modifiers on the resulting crystal shape in a mineralization reaction is well-established, the particular influence, for example, of the elemental doping on an atomic level is not easy to understand. The presence of citrate or acetate anions during the mineralization is expected to block the growth on distinct crystal planes.[22] However, this is not the only aspect in which carboxylate anions influence the mineralization process. The equilibrium of the hydrolytic reaction is likewise affected by citrate or acetate, given that they act as complexing agents for the zinc ions and alter the concentration of free ions in the solution.[23] The employment of ethanol/water mixtures was broadly studied in ZnO thin-film synthesis by means of chemical bath deposition (CBD).[24,25] Films consisting of densely oriented nanorod arrays with the *c* axis perpendicular to the substrate are fabricated in aqueous solution. When ethanol is added to the solvent, the crystals become randomly oriented in the films. This effect, however, has not yet been investigated for particle synthesis.[10,20]

In this work, we describe the synthesis of cobalt-doped zinc oxide single crystals, which feature the morphology of hexagonal platelets. The formation of these hexagons is controlled by a defined combination of growth modification parameters, that is, firstly the ratio of the employed solvent mixture and secondly the introduction of a dopant into the crystal lattice. The employed reaction conditions, in particular, inhibit twinning, which is otherwise frequently observed in zinc oxide-based particles. Our findings suggest that the impact of the dopant is not due to an electrostatic effect, whereby impurities are adsorbed on surface planes during the growth of the crystal as suggested by other groups.[26,27] Instead, the specific reaction sequence for mineralization of zinc oxide, which proceeds in solution at low temperatures (i.e., below 100 °C) through the formation of layered basic acetates, which contain both cobalt and zinc, might be the key to understanding the development of the observed different crystal morphologies.[28–30] This process has to be differentiated from well-described studies that make use of solid-state transformation of powders or films of layered metal salts at elevated temperatures.[31,32]

Finally, the deposition of aligned monolayers containing micro-sized tile-type patterns of regular ZnO hexagons was attempted by the Langmuir–Blodgett deposition technique. The difference in surface tension between water and organic solvent induces a Marangoni flow, which carries the particles to the air/liquid interface.[33–35] Furthermore, the influence of the surface modifications with polyelectrolyte multilayers on glass substrates in the Langmuir–Blodgett deposition was investigated.

2. Results and Discussion

2.1. Mineraliztion reaction and analysis of zinc oxide formation mechanism

In this study, the formation of precipitates by hydrolytic reaction from solutions of zinc and cobalt acetates in ethanol/water mixtures in the presence of hexamethylenetetramine (HMTA) was investigated. Owing to the low solubility of both metal acetates in ethanol and to avoid local oversaturations, which lead to inhomogeneous reaction conditions, individual solutions of the educts were immediately combined at an elevated reaction temperature of 95 °C. Although this procedure is in general an established route for zinc oxide mineralization, the combination of cobalt addition and use of an ethanol/water mixture has not been investigated before.

With respect to the desired hexagonal platelet formation, the best results were obtained with bath temperatures of 95 °C. Higher bath temperatures did not cause apparent changes, whereas bath temperatures below 90 °C did not lead to cobalt doping and also caused a drastic increase in the total reaction time. The reaction mixture appeared clear at first. After 5 minutes, a fluffy, voluminous precipitate was formed, which remained until 15 minutes from the start of the reaction. Afterwards, the mixture continuously turned milky and became completely opaque after 30 minutes. The reaction was terminated after 60 minutes. This behavior already indicates a stepwise formation process. The color of the mineralization products depends on the reaction time. Precipitates up to reaction times of 30 minutes have an off-white color, whereas a greenish product is formed at longer reaction times, that is, at a minimum of 45 minutes.

Both solvent mixture and cobalt addition have an influence on the composition and the morphology of the resulting mineralization products (Figure 1). In pure water, rod-shaped twins are obtained, whether cobalt is added to the reaction solution or not (Figure 2a). However, almost no cobalt doping or incorporation was observed in precipitates processed from pure water. Variation of the ethanol/water proportion in the solvent mixture changes the aspect ratio of the hexagonal crystallites, whereby a volume ratio of ethanol/water of 70:30 is the opti-

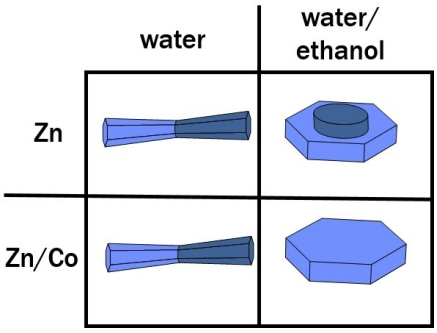

Figure 1. Simplified overview of the morphologies and twinning of mineralization products obtained in dependence of the metal ions in the reaction solution and the solvent. Only the combination of a water/ethanol solvent and the addition of cobalt successfully inhibits the otherwise typical twinning. Furthermore, significant cobalt incorporation is also observed only in water/ethanol mixtures.

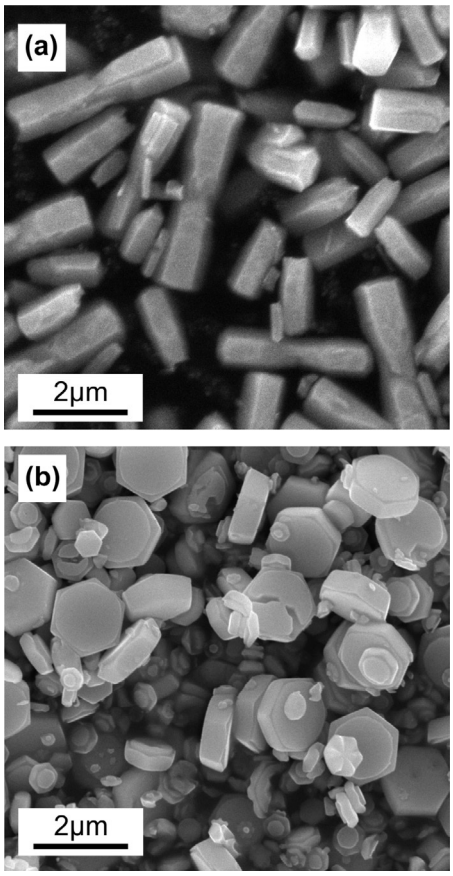

Figure 2. SEM images of mineralization products from solutions of zinc acetate (20 mM) and HMTA (100 mM) in (a) water and (b) an ethanol/water mixture (v/v, 70:30). The precipitates were isolated after 60 min reaction time.

mum for platelet formation with well-defined shapes. Higher ethanol contents lead to rounded features and spherical, non-single-crystalline particles. Without cobalt addition, only twins (hexagonal platelets with additional columnar features) are observed (Figure 2b). This important finding means that cobalt addition is mandatory for the formation of precipitates consisting of single-crystalline hexagonal platelets (Figure 3).

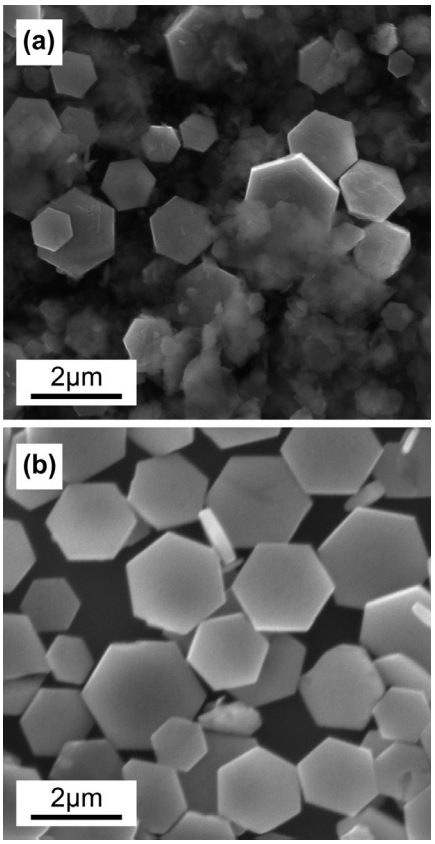

Figure 3. SEM images of mineralization products from solutions of zinc acetate (20 mM), cobalt acetate (1.2 mM) and HMTA (100 mM) in an ethanol/water mixture (v/v, 70:30) obtained at various reaction times. (a) 30 min and (b) 60 min.

The influence of the acetate anion and the use of HMTA as a means for generating the base were not investigated in detail in this study. Attempts were made to exchange the HMTA by solutions of ammonia in ethanol or methanol. However, this led to the formation of crystals with a completely different morphology and multiple types of twinning (Figure S1, Supporting Information). Furthermore, the substitution of the metal acetates by the corresponding nitrates resulted in the formation of smaller spherical particles (Figure S2, Supporting Information). It can be speculated that the moderate kinetics of the ammonia generation as a base formed from HMTA plays an important role in the ZnO formation process.

The mineralization products were obtained after prolonged reaction times (i.e., 60 min). Subsequently, the dependence of morphology and composition as a function of the reaction time was investigated. Samples were collected every 15 min by terminating the reaction through quenching the flask with the product mixture in an ice bath. Earlier reaction times could not be investigated because of the small amount of isolated precipitates formed during this period. Part of the precipitate consisted of a featureless haze, the quantity of which continuously decreased with prolonged reaction time (Figure 3a), while the amount of hexagonal platelets increased (Figure 3b).

To analyze the composition of the precipitates, X-ray diffraction measurements were carried out (Figure 4). At lower reac-

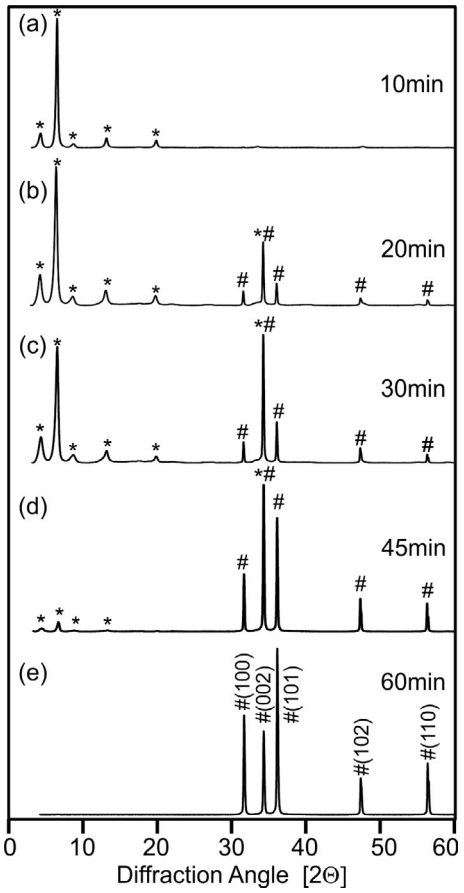

Figure 4. X-ray diffraction patterns of mineralization products from solutions of zinc acetate (20 mM), cobalt acetate (1.2 mM) and HMTA (100 mM) in an ethanol/water mixture (v/v, 70:30) obtained after various reaction times. (a) 10 min, (b) 20 min, (c) 30 min, (d) 45 min and (e) 60 min. Peaks are attributed to layered basic cobalt zinc acetate (asterisks) and zincite (hash marks). Miller indices in (e) correspond to zincite (JCPDS card no. 36-1451).

tion times, further components apart from cobalt-doped zinc oxide were formed. These contributions are attributed to layered basic metal acetates, which exhibit peaks with larger intensities at low diffraction angles (i.e., below $2\theta = 20^\circ$) originating from (00l) reflections.[36] However, a definite attribution to simple binary hydroxides such as β- or ε- zinc hydroxide or α- or β-cobalt(II) hydroxide was not possible.[37–39] In addition, a series of samples from mineralization reactions without the addition of cobalt was investigated (Figure S3, Supporting Information). The XRD pattern of the product from lower reaction times matches that of the heterometallic counterpart. However, the relative intensities of the different peaks varied significantly.

Based on the TEM investigations (see Section 2.3.), an attribution to a thin heterometallic layer, that is, a layered basic cobalt zinc acetate (LBCoZnA), seems reasonable. Cobalt-doped zinc oxide is exclusively observed in the X-ray diffractogram after prolonged reaction times (60 min).[40] The reaction is complete after 1 hour. No significant changes in the X-ray diffractogram were observed at prolonged reaction times and also after calcination at 300 °C (Figure S5, Supporting Information). In any case, peaks around 34° originate from both LBCoZnA and Co-doped ZnO but cannot be attributed to one component alone. With respect to the LBCoZnA, the peak at about 34° presumably corresponds to a (*hk*0) reflection. The contribution of basic salts becomes evident if samples obtained after reaction times below 45 minutes are subjected to calcination, which enforces the conversion to the single oxide. In this case, the (*hk*0) peak is drastically reduced in intensity. The preference of crystal growth along uncommon orientations was observed for layered basic mixed cobalt zinc salts in organic solvents.[41,42] This indicates that the employed solvent mixture does not only affect the morphology of the resulting Co-doped ZnO but all intermediate reaction stages as well, which underlines the complexity of this reaction.

The formation of basic salts and the incorporation of acetates in the precipitates, underpinning the idea of LBCoZnA formation, was confirmed by IR spectroscopy. A quantification of the amount of organic content was achieved by means of thermogravimetry coupled with mass spectroscopy (TG/MS).

IR spectra (Figure S6, Supporting Information) exhibited characteristic and very pronounced signals related to valence vibrations of the carboxylate group with ν_{as}(C–O) situated at approximately 1580 cm^{-1} and ν_s(C–O) at approximately 1410 cm^{-1}[32,39], but also contributions from rocking and deformation vibrations of the acetate backbone, for example, at 1336 and 1016 cm^{-1}.[43] In addition, Zn–O and O-Zn-O peaks at approximately 450–550 cm^{-1} were observed from samples obtained at longer reaction times. No evidence was found, however, regarding the formation of carbonate.[44]

Subsequently, the thermal decay was systematically studied by means of TG/MS (Figure S7, Supporting Information). The residual mass varies greatly for samples obtained at different reaction times. Samples synthesized at reaction times less than 1 hour exhibit a rather high mass loss upon annealing (up to 40%). The decay proceeds in several steps, in which water evolves at 70 and 146 °C. A major mass loss occurs between 220 and 290 °C, which corresponds to the pyrolysis of the acetate ions in the layered structure.[32,45] Accordingly, the evolution of CO and CO_2 can be observed with MS. Only samples synthesized at prolonged reaction times (>60 min) exhibit a lower mass loss of merely 2–3%. In this case, the thermal decay gradually proceeds and the decomposition steps are no longer recognizable.

2.2. Cobalt doping as studied by XRD, EPR, PL, and UV/VIS methods

The solubility of cobalt within the zincite lattice strongly depends on the particle size. This effect is a result of the polymorphism of CoO. Owing to the unfavorably higher surface energies of the rock salt relative to that of the wurtzite structure, CoO nanocrystals adopt the latter.[46] Whereas in Co-doped ZnO nanocrystals (<6 nm) concentrations of up to 30% cobalt with respect to the total metal content can be obtained, the amount in micrometer-sized crystals is limited to about 2%.[46,47] Thus, it is not surprising that the mineralization products, which exhibited no further crystalline phases in XRD studies, possess very little cobalt. Higher amounts of cobalt with re-

spect to zinc in the reaction solution did not lead to Co-doped ZnO with an increased cobalt content but instead prohibited the formation of the latter and a complex mixture of layered basic salts formed.

No evidence of cobalt was found in X-ray photoelectron spectroscopy (XPS) investigations, which indicates a concentration below the detection limit of $<1\,\%$ in regions close to the crystallite surface (about 3 nm depth). The employment of energy-dispersive X-ray spectroscopy (EDS) was also confronted with difficulties due to the low cobalt concentration of 1–2 % with respect to the total metal content. Furthermore, only a small shift of reflection positions in XRD can be expected according to Vegard's rule (Figure S4, Supporting Information).[48,49] Nevertheless, the incorporation of cobalt in the wurtzite structure, that is, the formation of Co-doped ZnO, is unambiguously proven by spectroscopic techniques as shown in the following.

The light-green precipitate exhibits peaks related to d–d transition levels in the UV/VIS spectrum (Figure 5 a). This verifies that Co^{2+} ions are occupying tetrahedral lattice positions and gives evidence that cobalt is substituting as Co^{2+} on zinc lattice sites in the wurtzite-type structure. The peaks are commonly attributed to the $^4A_2(F)\rightarrow{}^2E(G)$ (651 nm), $^4A_2(F)\rightarrow{}^4T_1(P)$ (608 nm) and $^4A_2(F)\rightarrow{}^2A_1(G)$ (564 nm) transitions, respectively.[40,50,51]

This finding is supported by photoluminescence (PL) (Figure 5 b) and electron paramagnetic resonance (EPR) (Figure 6) spectra. The PL spectra exhibit two signals, which are typical for ZnO; on the one hand, the exciton peak and on the other, a broader signal at higher wavelengths ("green luminescence"), which is caused by defect states.[49,52,53] Doping with Co^{2+} leads to a significantly reduced intensity of the latter because the intrinsic defect concentration is lower than that of pure zinc oxide.[52] This influence of the dopant is even more visible in the EPR spectra (Figure 6). The EPR spectrum of pure ZnO exhibits one sharp signal at 350 mT ($g=1.96$) originating from core defect states within the ZnO lattice. No other contributions, for example, from surface defects or impurities, were detected. However, this signal is completely suppressed in samples of Co-doped ZnO, which is a direct proof for incorporation of the Co^{2+} in the zincite lattice.[52,54,55] At room temperature, no contributions of signals related to Co^{2+} were evident, given that such signals are typically observed only at very low temperatures (i.e., about liquid helium temperature) for Co-doped ZnO species. By using EPR spectroscopy, it is possible to distinguish substitutional from interstitial Co^{2+} ions. The substitutional ions (ground state $^4A_2(F)$, $S=3/2$) are characterized by an axial g-tensor ($g_\perp=2.292$, $g_\parallel=2.226$) and a large zero-field splitting $D=2.75\ cm^{-1}$, whereas the interstitials (ground state $^4T_1(\Gamma_7)$, $S=1/2$) yield a broad feature with $g_\parallel^{eff}\approx3$ and $g_\perp^{eff}\approx5$.[56,57] At higher temperatures, an increasing line broadening occurs, which leads to the disappearance of these contributions above 100 K. In the current investigation, two very broad signals were detected at a temperature of 80 K.[54,55]

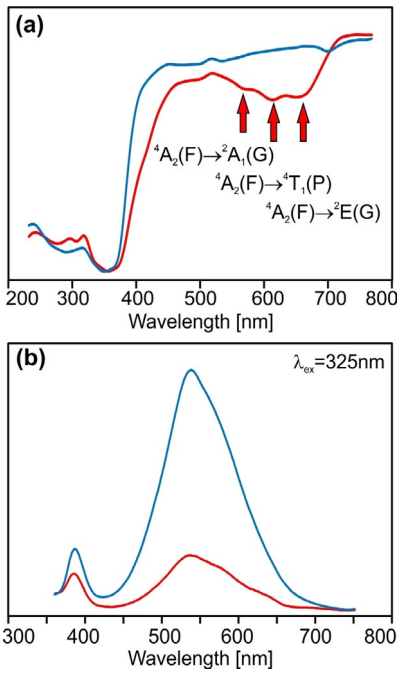

Figure 5. (a) UV/VIS spectra measured in reflection mode and (b) photoluminescence spectra of cobalt-doped (red) and undoped (blue) zinc oxide powders. Both samples were collected after 60 min reaction time.

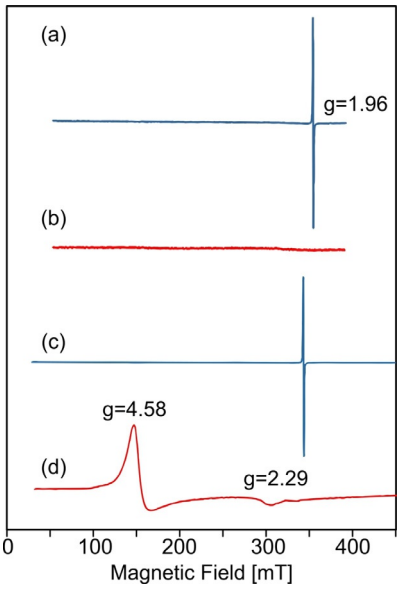

Figure 6. EPR spectra of mineralization products containing pure (blue) and Co-doped (red) zinc oxide at (a, b) room temperature and (c, d) with cooling at 80 K.

2.3. TEM investigation of hexagonal platelets and rod-shaped twins

The main focus of the performed TEM investigations is the verification of single crystallinity and the exclusion of twinning in the hexagonal platelets synthesized in ethanol/water solvent with cobalt addition (Figure 3 b). The precipitates were characterized in terms of morphology, cobalt content, surface coverage and (if applicable) the surrounding matrix. In doing so, mineralization products obtained after reaction times ranging

from 15 to 60 min were examined, as well as hexagonal platelets, which were subjected to an additional annealing step. Furthermore, the rod-shaped twins obtained from pure water solvent (Figure 2a) were investigated with respect to their twinning configuration.

As shown in Figure 7, the mineralization products after 15 min reaction time already contain platelets with a distinctively hexagonal morphology although their surface appears rough and irregular. Selected area electron diffraction (SAED) indicates single crystallinity and verifies the platelets' surface being perpendicular to the *c* axis (Figure S9a, Supporting Information); hence, surface and bottom correspond to {001} lattice planes. The terminating planes on the side are {110} and {2$\bar{1}$0} type or, in order to reflect their equivalent symmetry, {1$\bar{2}$10} in Bravais notation. The hexagonal platelets are embedded in a partly amorphous, nanocrystalline matrix, which is interpreted as the opaque haze described in Section 2.1 and attributed to LBCoZnA and nanocrystalline ZnO (Figure S9b, Supporting Information). This is consistent with the observation that a prolonged reaction time of 45 min leads to a significant decrease in accompanying matrix material, while the amount of well-defined hexagonal platelets is increased (Figure 8a). The platelets do not only exhibit a more even surface, but they also appear more often in almost an ideal, highly symmetrical hexagonal shape. Nevertheless, they typically feature a haze-like, partly crystalline surface coverage, which is seen as a residual phase from the matrix material (Figure 8b). This interpretation is underpinned by EDS measurements showing a cobalt-rich composition notably different to the platelets. As shown in Figure 8c, this surface coverage is eliminated by an additional annealing step at 300 °C. Furthermore, the removal of those matrix residuals is accompanied by an increase in surface smoothness and hence the general quality of the hexagonal platelets. Although contrast variations were observed in some hexagons indicating minor structural defects, no enrichment or secondary phases of cobalt were observed by scanning transmission electron microscopy (STEM) investigations (Figure S10, Supporting Information). Thus, within our detection limits, the hexagons appear as chemically homogeneous with cobalt concentrations below 1%, which is slightly lower than that expected from other measurements (Section 2.2).

Given that some special cases of twinning, such as a rotation-free *c*-axis inversion, would not be detectable by SAED in a [001] zone-axis condition, cross-sections of the hexagonal platelets were prepared allowing a direction of view along $<100>$. The respective HRTEM images showed no indication for any kind of inner grain boundary (Figure 8d). A qualitative comparison of reflection intensities in microdiffraction measurements can be used to determine the polarity and hence the absolute orientation of such non-centrosymmetric crystals as zinc oxide.[58] Thus, convergent beam electron diffraction

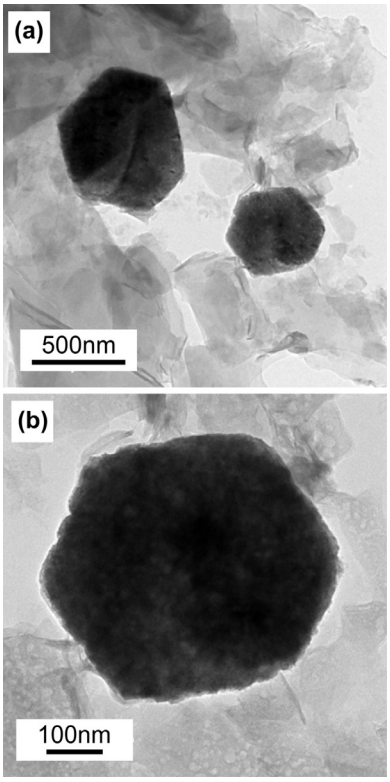

Figure 7. TEM images of mineralization products from solutions of zinc acetate (20 mM), cobalt acetate (1.2 mM) and HMTA (100 mM) in an ethanol/water mixture (v/v, 70:30) obtained after 15 min. (a) Overview image of hexagonal platelets surrounded by matrix material. (b) Top-view image of a hexagonal platelet in [001] orientation.

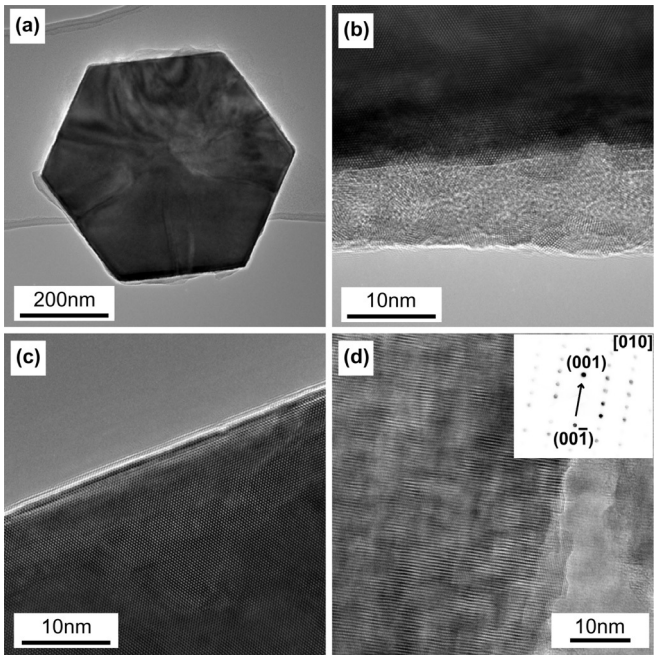

Figure 8. TEM images of mineralization products from solutions of zinc acetate (20 mM), cobalt acetate (1.2 mM) and HMTA (100 mM) in an ethanol/water mixture (v/v, 70:30) obtained after 45 min. (a) Top-view image of a hexagonal platelet in [001] orientation and (b) HRTEM image of the platelet's edge, revealing a surface coverage by haze-like matrix residuals. (c) HRTEM image of a platelet's edge isolated after 45 min reaction time and subsequent to an additional calcination in air at 300 °C. (d) HRTEM image showing the cross-section of a hexagonal platelet and the corresponding CBED pattern, which depicts the direction of the *c* axis. No other orientation or indication for inner grain boundaries were observed. (A survey image of the entire crystallite is included in the Supporting Information as Figure S8).

(CBED) measurements were performed to check if any *c*-axis inversion is present inside the hexagonal platelets. As exemplarily shown by the inset in Figure 8d, the same orientation was found for the entire hexagonal crystal. Based on these findings and the SAED patterns, twinning is excluded, thus identifying the crystals as being perfect single-crystalline hexagons.

In contrast to the hexagonal platelets, the rod-shaped precipitates indicate (inversion) twinning already by their morphology with symmetric conical narrowing towards the center of the elongated crystals, which reflects respective growth characteristics and hence crystallographic orientation (insets in Figure 9). HRTEM and STEM imaging of cross-sections reveal a semi-coherent, slightly meandering interface, which is predominantly free from secondary phases (Figure 9a,c). Beside minor amounts of an unspecifiable amorphous C-containing phase, neither grain-boundary films nor cobalt segregation were observed at the interface. To verify the presumed inversion twinning, the previously described CBED method for the determination of absolute *c*-axis directions was also applied for the rod-shaped crystals. As revealed by the different intensities of the {002} reflections in Figure 9b, the crystal features a $[00\bar{1}] \| [00\bar{1}]$ tail-to-tail inversion of the *c* axis. Although all investigated rod-shaped twins exhibited this type of twinning, a $[001] \| [001]$ head-to-head configuration or other measurable deviations were never observed. Annular bright field STEM (ABF-STEM) allows the effective visualization of light elements such as oxygen atoms, which are otherwise indiscernible. Thus, the absolute orientation of the polar *c* axis, which is crystallographically determined by the stacking of Zn- and O-layers in the unit cell, can be directly concluded from respective high-resolution images. Although adjacent zinc- and oxygen-atom columns are hardly resolvable, they appear in [010] zone axis orientation as elongated ellipsoids. As shown in Figure 9d, ABF-STEM images verify a $(00\bar{1}) \| (00\bar{1})$ tail-to-tail orientation for the rod-shaped nanotwin, which is further confirmed by quantitative STEM image simulations (Figure 9e).[59]

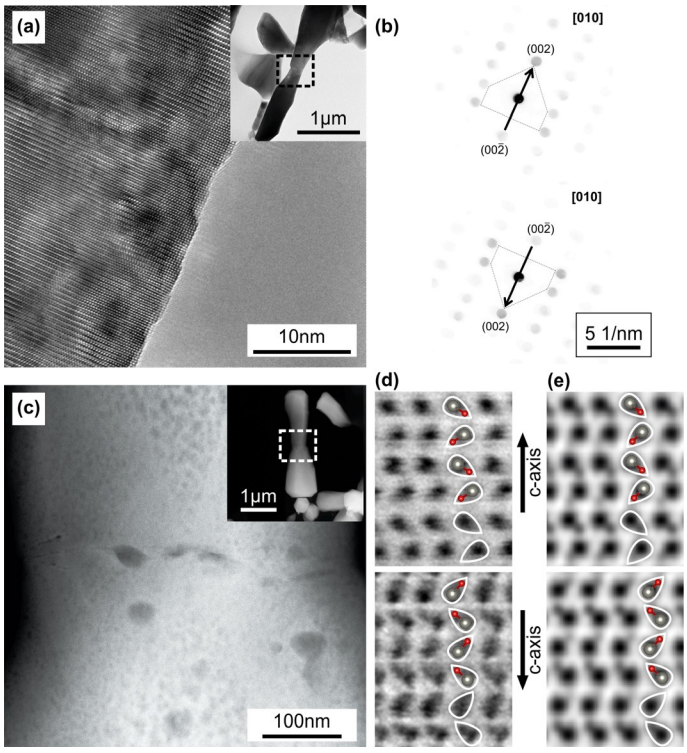

Figure 9. (a) Fourier-filtered high-resolution transmission electron microscopy (HRTEM) image of the interface of a rod-shaped twin in [010] zone-axis orientation. No interlayer is present. The inset shows a survey, and the dashed black rectangle indicates the area investigated in the magnification. (b) CBED pattern from opposite sides of the twin boundary. The different intensities of the reflection discs in the CBED images, especially between (002) and (00$\bar{2}$), indicate the direction of the *c* axis and hence a tail-to-tail inversion twin boundary. (c) High-angle annular dark field (HAADF)-STEM images of a rod-shaped twin; in [010] zone-axis orientation. The dashed white rectangle in the inset indicates the area investigated in the magnification. (d) ABF-STEM visualization of the Zn-O ellipsoids above and below the grain boundary indicating the direction of the polar *c* axis, and (e) corresponding image simulations.

The reason for the ubiquitously observed twinning of zinc oxide is the subject of manifold research. The presence of an organic template might facilitate twin formation but is by no means essential.[60–62] Moreover, twins and multiples are not exclusively formed in solution but also in gas-phase processes.[63–65] However, in the case of tail-to-tail twinning with a straight $(00\bar{1}) \| (00\bar{1})$ interface, the opposed boundary surfaces are oxygen-terminated, which demands some kind of interlayer to permit bonding. Hence, it is plausible to assume a template for the rod-shaped twins at least at the early stages, when the seed crystal for the twin is formed. No distinctive indications for that were found in the TEM investigations, though. It remains unclear if the C-containing phase detected at the boundary is a residual from an organic template. Ultimately, it can be stated that the tendency to form twins is a characteristic property of the wurtzite structure, which favors a variety of twinning modes.[66,67]

2.4. Langmuir–Blodgett deposition of hexagonal platelets of crystalline ZnO

The Langmuir–Blodgett (LB) technique was historically established for films of amphiphilic organic molecules, but the formation of monolayers and successful deposition of inorganic nano-objects such as spherical nanoparticles and nanowires was demonstrated in recent years.[68] The strategy for monolayer formation of inorganic nano-objects on the aqueous subphase typically mimics the fabrication of films of the archetypical amphiphiles. Thus, the employed route makes use of either hybridization through organic molecules or direct spreading of inorganic nano-sized objects dispersed in solvents immiscible with water.[68,69]

In our study, a fundamentally different approach was applied that does not require the addition of organic surfactants or immiscible organic solvents; instead an aqueous dispersion of the hexagonal platelets was prepared by prolonged ultrasound sonification. The Co-doped ZnO was calcined at 300 °C prior to the slurry preparation to remove carboxylate residues on the surface. The ultrasound treatment allowed a complete dissipation of soft agglomerates without breaking or corruption of the hexagonal platelets. The resulting dispersion was cast into

the trough of the LB set-up. Dropwise addition of various alcohols induced a Marangoni flow in the dispersion with the movement being visible to the naked eye. The magnitude of the flow was influenced by the alkyl chain length of the added alcohol, which corresponded to earlier investigation of the mixing process.[70] In this way, the crystallites were transported to the liquid/air interface and a layer formed on the surface of the aqueous subphase. We found that *n*-butanol or *n*-pentanol produced the best layers with respect to uniformity and surface coverage. More polar alcohols such as methanol or ethanol instead lead to the formation of agglomerates and "islands" on the liquid surface. The resulting difference in compression behavior is directly reflected in the corresponding surface pressure (Π) versus surface area (A) isotherms (Figure 10a). Compression of the particulate layer resulted in an increase of the particle density spread on the surface and also caused the generation of more closely packed structures (Figure S11, Supporting Information). The efficiency of LB film formation strongly depended on the monolayer surface pressure. In general, the deposition of LB films was inefficient at surface pressures below 10 mN m^{-1}.

The transfer of the particulate layer to the glass surface with a polyelectrolyte multilayer (PEM) modification was investigated in detail. The substrate was extracted from the dispersion, whereby constant surface pressure was maintained by narrowing of the barriers of the LB trough. The formation of the particulate layer by addition of an alcohol to the aqueous subphase was mandatory for obtaining a coating of the substrate in the following transfer process. Therefore, a simple dip-coating process did not result in any sufficient coverage of the substrate. Glass substrates were coated with PEMs consisting of stacked layers of polyethyleneimine (PEI), poly(sodium 4-styrenesulfonate) (PSS) and poly(allylamine hydrochloride) (PAH).[71] Coatings of Co-doped ZnO were obtained on PEM stacks with both anionic (PEI/PSS)(PAH/PSS)$_2$ and cationic (PEI/PSS)(PAH/PSS)$_2$(PAH) termination. No major influence on the morphology of the coatings was visible. SEM images (Figure 10b) showed that the surface coverage was incomplete in all cases and revealed larger gaps between well-coated areas. Furthermore, tessellation formed only in very small patches consisting of a maximum of 12–14 crystallites. Interestingly, no deposition at all was observed when the glass substrate was not modified by PEM.

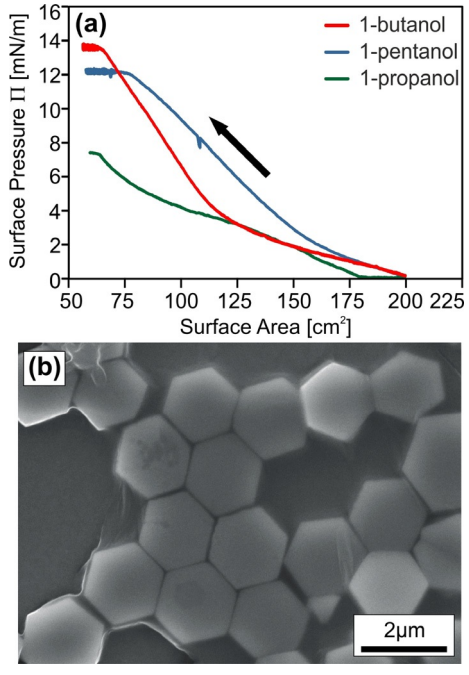

Figure 10. (a) Typical surface pressure–area (Π–A) behavior for LB trough experiments using various dispersant alcohols. Collapse of the material layer is characterized by a deviation from linearity. The compression progresses from right to left. (b) SEM image showing tessellation of hexagonal platelets of cobalt-doped zinc oxide on a glass substrate modified with (PEI/PSS)(PAH/PSS)$_2$.

Piezoresponse force microscopy (PFM) as well as Kelvin probe force microscopy (KPFM) investigations were carried out (Figures 11 and S12, Supporting Information). These methods are able to provide information about the crystallographic orientation of the crystallites on the substrate.[72,73] The inferior adhesion of the individual ZnO crystallites may cause major problems due to loosening and shifting of the particles. Redundant material was removed carefully with a polydimethylsiloxane (PDMS) stamp prior to the PFM measurements. Best results were obtained for Co-doped ZnO platelets immobilized on a glass substrate with (PEI/PSS)(PAH/PSS)$_2$(PAH) termination (Figure 11). Several hexagonally shaped platelets were identified in the topography (Figure 11a) and the corresponding deflection image (Figure 11b). The platelets had a diameter of about 700 nm and a height of around 100 nm. Protrusions, which are sometimes visible on the predominantly flat tops of the studied platelets, indicate contaminations from the preparation process. The corresponding deflection image was able to confirm the topographic contours. A clear piezoresponse at the platelet positions was observed from the PFM amplitude and phase images in Figures 11c,d. The PFM response was strongest at the bottom and almost vanishing at the upper part of the platelets. The maximum response amplitude was in the order of about 70 pm at a PFM driving voltage amplitude of 30 V. Assuming that the *c* axis of Co-doped ZnO is oriented perpendicular to the top surface of the platelets, a piezo-coefficient of $d_{33} \approx 2.3$ pm V^{-1} was deduced. This rather low value might be a consequence of local contaminations, which reduce the mechanic coupling between the AFM tip and the surface of the single-crystalline platelet. It should also be noted that doping with Co^{2+} is known to reduce the piezoresponse in the order of 10–20% relative to that of undoped ZnO.[74,75] Furthermore, values would be lower for ZnO platelets as for rod-shaped crystallites.[76]

In the KPFM measurements, no influence of the terminal PEM layer became evident, given that a positive surface charge was detected in all cases (Figure S12, Supporting Information). Although the coating consists of single crystals, the deposition process is not controlled by the orientation of the polar axis in the crystallites but presumably by the electrokinetic potential of the particles in water. This view was supported by zeta-potential measurements. The zeta potential of dispersions of annealed Co-doped ZnO decreased within 5–10 minutes from

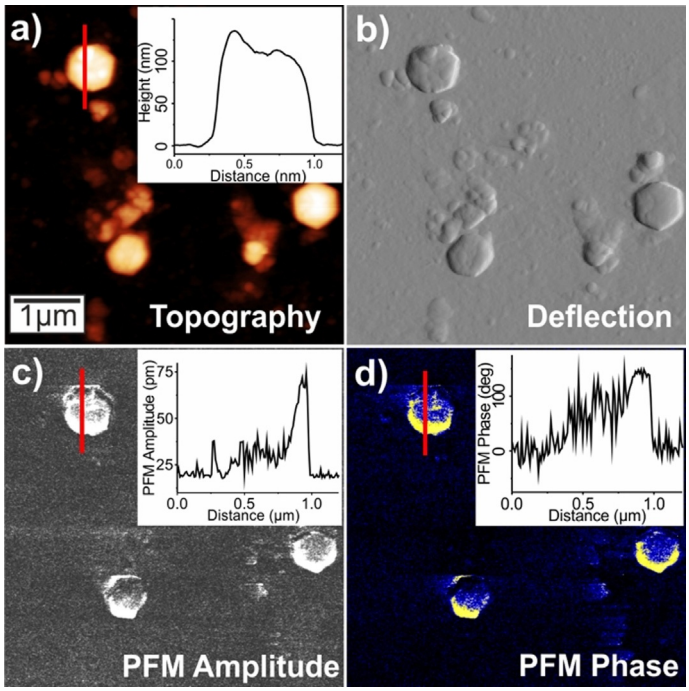

Figure 11. (a) AFM topography image (*z*-scale: 120 nm) and (b) corresponding deflection image to highlight topography contours. (c) Corresponding PFM amplitude image (*z*-scale: 30 pm) and (d) PFM phase image (*z*-scale: 180°). The insets are cross-sectional profiles along the red lines indicated in the images.

about +30 to ±0 mV, which corresponds to earlier investigations on undoped ZnO.[77] This shift is due to continuous dissolution of Zn^{2+}(aq) from the zinc oxide, leading to a compression of the electrical double layer of the colloidal particles.

3. Conclusion

The precipitation of undoped zinc oxide from solutions of zinc acetate in the presence of HMTA at elevated temperatures proceeds in two distinct steps. Initially, layered basic zinc acetate (LBZA) is formed, which is subsequently converted into zinc oxide. This route is well-investigated and established.[28] The intermediate LBZA is a stable compound and can be isolated without problems. In fact, the conversion of LBZA to ZnO was studied.[28,29] The mechanism for the concerted dissolution and recrystallization step from LBZA to ZnO is, however, currently not completely understood. Modification of the reaction conditions can lead to the isolation of mineralization products, in which LBZA and ZnO are found in immediate proximity in multicomponent particles.[78–80] The solvent, however, plays an important role in this process. Whereas rod-shaped crystallites are obtained in water, the use of *n*-butanol or ethanol/water mixtures allows the formation of platelet-shaped particles (independently whether zinc acetate/HMTA[10,18] or LBZA[28,29] are chosen). In all these cases, twinning is always observed in undoped zinc oxide.

The addition of Co^{2+} ions to the zinc acetate/HMTA solution leads to the formation of a layered basic cobalt zinc acetate (LBZnCoA) as reaction intermediate. This later converts to cobalt-doped zinc oxide. Moreover, if carried out in ethanol/water mixtures, this route effectively prohibits twinning of the resulting Co-doped ZnO hexagonal platelets. In other words, the formation of single crystals is directly related to the nature of the intermediate phase (Figure 12).

This contradicts alternative suggestions about the influence of doping on the resulting crystal shape in the mineralization process.[26,27] Often a face-selective electrostatic crystal growth inhibition is claimed, whereby the dopants are inserted inside the lattice of a host crystal and continuously change the energy of active facets and consequently affect the growth pattern.[26,81] This view might be applicable for other compounds or different reaction conditions, such as a much higher pH or an addition of multidentate complexing agents. However, the specific reaction route for the formation of ZnO and the resulting crystal shape at lower pH values by using HMTA must be assessed by a more comprehensive model for the underlying mechanism.

4. Experimental Section

4.1. Mineralization reaction

Zinc acetate dihydrate (0.439 g, 2 mmol) and cobalt acetate tetrahydrate (0.030 g, 0.12 mmol) were dissolved in demineralized water (70 mL). In a second vessel, HMTA (1.400 g, 10 mmol) was dissolved in absolute ethanol (30 mL). The aqueous solution of the metal salts was transferred to a two-neck flask with a reflux condenser and inserted carefully in a preheated oil bath (95 °C). After 5 min, the second solution was added with a funnel in one batch. The mineralization was terminated by removing the flask from the oil bath and carefully quenching it in an ice bath. The product was isolated by centrifugation and washed one time with water/ethanol (i.e., by shaking the sediment in the centrifugation tube with fresh solvent). The centrifugation tube was subsequently stored in a drying cabinet at a maximum of 40–45 °C overnight. Care was taken not to exceed this range because the moist

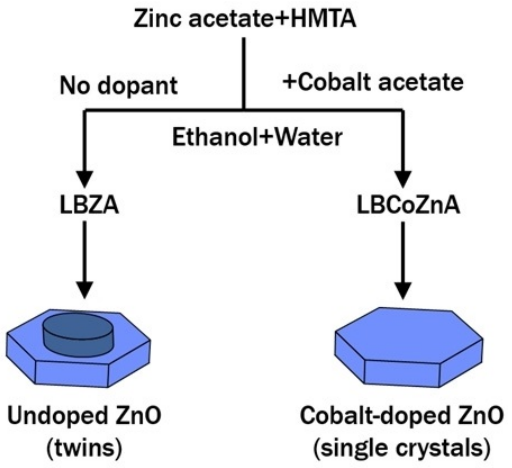

Figure 12. Schematic presentation of the stepwise formation of ZnO or Co-doped ZnO via the corresponding intermediates and their influence on the twin formation.

product is prone to undesired side reactions at higher temperatures. The product can be isolated in the form of a greenish powder (about 70–100 mg). Further treatment involved calcination at 350 °C in a furnace in air, which did not cause any evident change in color or morphology.

4.2. Langmuir–Blodgett deposition

Coating of substrates with monolayers was carried out with a commercially available Langmuir–Blodgett deposition trough (KN 2002, KSV Nima). The system is equipped with automated barriers and allows control over a Wilhelmy balance. The cobalt-doped zinc oxide powder (25 mg) was sonicated (Q500 Sonicator, Fisherbrand) in water (190 mL) for 10 min. Care was taken to avoid excessive heating. The suspension was poured into the deposition trough, and an alcohol (e.g., *n*-butanol, 2–6 mL) was added dropwise over a period of 10 to 15 min by using a syringe. The surface flow induced by each drop was allowed to expire. A slide of PEM-modified glass (about $40\times25\ mm^2$) was immersed (20 mm) thereafter. LB coatings were prepared by compressing the particulate layer to a surface pressure of 10–15 $mN\,m^{-1}$. The slide was subsequently extracted at a rate of 2.5 $mm\,min^{-1}$.

4.3. Characterization techniques

Instrumentation and sample preparation: Thermogravimetry (TG-IR): TG209F1-Iris (Netzsch) coupled with a QMS403C-Aëolos mass spectrometer (Bruker). Samples were measured under oxygen at a heating rate of 10 °C min^{-1} in the range of 30–600 °C in aluminium crucibles. Zeta-potential measurements: Zetasizer Nano (Malvern). Samples were measured in 10 mm quartz cuvettes. IR spectroscopy: Nicolet 6700 (ThermoScientifc). Powders were measured with an attenuated total reflection (ATR) unit. X-ray diffraction (XRD): Miniflex 600 (Rigaku), $Cu_{K\alpha}$ radiation, 600 W in Bragg–Brentano geometry. Scanning electron microscopy (SEM): Micrographs were obtained with an XL Series, Philips, XL30 FEG. Photoluminescence (PL): Spectra were recorded by using a Fluorolog-3 (Horiba) with a Xenon lamp and an excitation wavelength of 325 nm.

Electron paramagnetic resonance (EPR): Continuous wave (cw) X-band (9.86 GHz) EPR measurements were performed at room temperature with a Bruker EMX spectrometer using a cylindrical super-high-quality (SHQ) resonator (Bruker). The offset in the magnetic field and the exact *g*-factors in X-band measurements were determined with a polycrystalline DPPH (2-diphenyl-1-picrylhydrazyl) reference sample with a well-known *g*-factor ($g=2.0036$). The EPR spectral analysis was performed with the aid of the WINEPR program from Bruker. A turbo molecular pump was used to evacuate the EPR quartz tubes.

Transmission electron microscopy (TEM): For studies of powders, ethanol suspensions of the respective mineralization products were dispersed in an ultrasonic bath for 10 min. One drop of each suspension was deposited on a TEM grid with a supporting holey carbon film (400 mesh, copper, Plano, Wetzlar, Germany). Cross-sections of hexagonal platelets and rod-shaped twins were prepared by embedding the sample material in epoxy resin and cutting out a 3 mm disc, which was mechanically polished down to a thickness below 20 μm. Subsequently, the disc was mounted on a TEM grid (200 mesh, copper, Plano, Wetzlar, Germany) and argon-ion milled (DuoMill 600, Gatan, Pleasanton, CA, USA) until electron transparency was reached. The TEM investigations were performed by using a JEOL JEM 2100F as well as a JEOL JEM ARM 200F (JEOL, Tokyo, Japan) with a spherical aberration corrector (C_s corrector), both equipped with an energy dispersive X-ray spectroscopy (EDX) system (JEM 2100F: TEM 250 SDD, Oxford Instruments, Wiesbaden, Germany; ARM 200F: JED 2300T, JEOL, Tokyo, Japan).

Piezoresponse force microscopy: For PFM, an Asylum Research MFP-3D atomic force microscopy (AFM) system was employed. The system equipped with an $80\times80\ \mu m^2\times10\ \mu m$ closed loop scanner was modified with an external voltage amplifier (F10A from FLC Electronics AB, Partille (SWE)) to extend the applicable voltage range. For the PFM measurements, ASYELEC-01-R2 probes with conductive Ti/Ir tip coating from Asylum Research (Santa Barbara, CA (USA)) were used. These probes have a typical tip curvature radius of 25 ± 10 nm and a spring constant of $k\approx2.8\ N\,m^{-1}$. The applied PFM driving voltage amplitude was varied in the range of 10 to 40 V and the frequency was set to 9 kHz well below the cantilever's resonance ($f_{res}\approx75$ kHz). The applied normal load was in the order of 12 nN.

Acknowledgements

Support of our research was made possible through the Deutsche Forschungsgemeinschaft within DFG PAK 926 (SCHN 375 34-1).

Conflict of interest

The authors declare no conflict of interest.

Keywords: cobalt · crystallization · doping · Langmuir–Blodgett films · mineralization · zinc oxide

[1] T. Ohtake, *Mol. Syst. Des. Eng.* **2018**, *3*, 804–818.
[2] M. Niederberger, *Adv. Funct. Mater.* **2017**, *27*, 1703647.
[3] A. Kolodziejczak-Radzimska, T. Jesionowski, *Materials* **2014**, *7*, 2833–2881.
[4] D. Lincot, *MRS Bull.* **2010**, *35*, 778–789.
[5] P. K. Kannan, D. J. Late, H. Morgan, C. S. Rout, *Nanoscale* **2015**, *7*, 13293–13312.
[6] T. D. Clark, R. Ferrigno, J. Tien, K. E. Paul, G. M. Whitesides, *J. Am. Chem. Soc.* **2002**, *124*, 5419–5426.
[7] T. D. Clark, J. Tien, D. C. Duffy, K. E. Paul, G. M. Whitesides, *J. Am. Chem. Soc.* **2001**, *123*, 7677–7682.
[8] R. Z. Ma, M. Osada, L. F. Hu, T. Sasaki, *Chem. Mater.* **2010**, *22*, 6341–6346.
[9] S. Cho, J. W. Jang, S. H. Jung, B. R. Lee, E. Oh, K. H. Lee, *Langmuir* **2009**, *25*, 3825–3831.
[10] M. Wang, S. H. Hahn, J. S. Kim, J. S. Chung, E. J. Kim, K. K. Koo, *J. Cryst. Growth* **2008**, *310*, 1213–1219.
[11] N. Qin, Q. Xiang, H. B. Zhao, J. C. Zhang, J. Q. Xu, *CrystEngComm* **2014**, *16*, 7062–7073.
[12] S. Hussain, T. M. Liu, M. Kashif, S. X. Cao, W. Zeng, S. B. Xu, K. Naseer, U. Hashim, *Mater. Lett.* **2014**, *128*, 35–38.
[13] K. Ada, M. Gökgöz, M. Önal, Y. Sankaya, *Powder Technol.* **2008**, *181*, 285–291.
[14] M. R. Alenezi, A. S. Alshammari, T. H. Alzanki, P. Jarowski, S. J. Henley, S. R. P. Silva, *Langmuir* **2014**, *30*, 3913–3921.
[15] Z. Xue, Z. Cheng, Q. Xiang, X. Wang, J. Xu, *ACS Appl. Mater. Interfaces* **2017**, *9*, 41559–41567.
[16] J. Xu, Z. Xue, N. Qin, Z. Cheng, Q. Xiang, *Sens. Actuators B* **2017**, *242*, 148–157.
[17] S. Zhang, L. Chen, R. X. Shi, Y. N. Zhu, P. Yang, *J. Nanosci. Nanotechnol.* **2017**, *17*, 754–760.
[18] O. Carp, A. Tirsoaga, R. Ene, A. Ianculescu, R. F. Negrea, P. Chesler, G. Ionita, R. Birjega, *Ultrason. Sonochem.* **2017**, *36*, 326–335.
[19] A. S. Huang, J. Caro, *J. Cryst. Growth* **2010**, *312*, 947–952.
[20] R. Y. Zhang, M. Hummelgard, H. Olin, *Mater. Sci. Eng. B* **2014**, *184*, 1–6.

[21] N. Mala, K. Ravichandran, S. Pandiarajan, N. Srinivasan, B. Ravikumar, K. C. S. Pushpa, K. Swaminathan, T. Arun, *Ceram. Int.* **2016**, *42*, 7336 – 7346.
[22] K. L. Meagley, S. P. Garcia, *Cryst. Growth Des.* **2012**, *12*, 707 – 713.
[23] S. Das, K. Dutta, A. Pramanik, *CrystEngComm* **2013**, *15*, 6349 – 6358.
[24] M. S. Wang, S. H. Hahn, J. S. Kim, S. H. Hong, K. K. Koo, E. J. Kim, *Mater. Lett.* **2008**, *62*, 4532 – 4534.
[25] M. S. Wang, E. J. Kim, E. W. Shin, J. S. Chung, S. H. Hahn, C. Park, *J. Phys. Chem. C* **2008**, *112*, 1920 – 1924.
[26] A. K. Guria, N. Pradhan, *Chem. Mater.* **2016**, *28*, 5224 – 5237.
[27] J. Joo, B. Y. Chow, M. Prakash, E. S. Boyden, J. M. Jacobson, *Nat. Mater.* **2011**, *10*, 596 – 601.
[28] X. Chen, X. Y. Song, W. Qiao, X. Zhang, Y. Sun, X. B. Xu, W. Zhong, Y. W. Du, *CrystEngComm* **2016**, *18*, 9139 – 9151.
[29] J. Demel, J. Pleštil, P. Bezdička, P. Janda, M. Klementová, K. Lang, *J. Colloid Interface Sci.* **2011**, *360*, 532 – 539.
[30] M. K. Liang, M. J. Limo, A. Sola-Rabada, M. J. Roe, C. C. Perry, *Chem. Mater.* **2014**, *26*, 4119 – 4129.
[31] P. Gerstel, R. C. Hoffmann, P. Lipowsky, L. P. H. Jeurgens, J. Bill, F. Aldinger, *Chem. Mater.* **2006**, *18*, 179 – 186.
[32] T. Shinagawa, M. Watanabe, T. Mori, J. I. Tani, M. Chigane, M. Izaki, *Inorg. Chem.* **2018**, *57*, 13137 – 13149.
[33] Y. Cai, B. M. Z. Newby, *J. Am. Chem. Soc.* **2008**, *130*, 6076 – 6077.
[34] A. Domínguez, P. Malgaretti, M. N. Popescu, S. Dietrich, *Phys. Rev. Lett.* **2016**, *116*, 078301.
[35] H. Kim, K. Muller, O. Shardt, S. Afkhami, H. A. Stone, *Nat. Phys.* **2017**, *13*, 1105 – 1110.
[36] G. G. C. Arizaga, K. G. Satyanarayana, F. Wypych, *Solid State Ionics* **2007**, *178*, 1143 – 1162.
[37] Z. A. Hu, Y. L. Xie, Y. X. Wang, L. J. Xie, G. R. Fu, X. Q. Jin, Z. Y. Zhang, Y. Y. Yang, H. Y. Wu, *J. Phys. Chem. C.* **2009**, *113*, 12502 – 12508.
[38] Z. P. Liu, R. Z. Ma, M. Osada, K. Takada, T. Sasaki, *J. Am. Chem. Soc.* **2005**, *127*, 13869 – 13874.
[39] L. Poul, N. Jouini, F. Fievet, *Chem. Mater.* **2000**, *12*, 3123 – 3132.
[40] M. Gaudon, O. Toulemonde, A. Demourgues, *Inorg. Chem.* **2007**, *46*, 10996 – 11002.
[41] J. T. Rajamathi, N. Ravishankar, M. Rajamathi, *Solid State Sci.* **2005**, *7*, 195 – 199.
[42] B. Wang, H. Lin, Z. Yin, *Mater. Lett.* **2011**, *65*, 41 – 43.
[43] M. K. Johnson, D. B. Powell, R. D. Cannon, *Spectrochim. Acta Part A* **1981**, *37*, 899 – 904.
[44] M. C. Hales, R. L. Frost, *Polyhedron* **2007**, *26*, 4955 – 4962.
[45] E. Hosono, S. Fujihara, T. Kimura, H. Imai, *J. Colloid Interface Sci.* **2004**, *272*, 391 – 398.
[46] C. C. Ma, A. Navrotsky, *Chem. Mater.* **2012**, *24*, 2311 – 2315.
[47] B. B. Straumal, A. A. Mazilkin, S. G. Protasova, P. B. Straumal, A. A. Myatiev, G. Schütz, E. Goering, B. Baretzky, *Phys. Met. Metallogr.* **2012**, *113*, 1244 – 1256.
[48] V. Gandhi, R. Ganesan, H. H. Abdulrahman Syedahamed, M. Thaiyan, *J. Phys. Chem. C* **2014**, *118*, 9715 – 9725.
[49] A. Hassanpour, P. Guo, S. Shen, P. Bianucci, *Nanotechnology* **2017**, *28*, 435707.
[50] P. Koidl, *Phys. Rev. B* **1977**, *15*, 2493 – 2499.
[51] M. Shatnawi, A. M. Alsmadi, I. Bsoul, B. Salameh, G. A. Alna'washi, F. Al-Dweri, F. El Akkad, *J. Alloys Compd.* **2016**, *655*, 244 – 252.
[52] R. Baraki, P. Zierep, E. Erdem, S. Weber, T. Granzow, *J. Phys. Condens. Matter* **2014**, *26*, 115801.
[53] B. Panigrahy, M. Aslam, D. Bahadur, *J. Phys. Chem. C* **2010**, *114*, 11758 – 11763.
[54] A. Savoyant, H. Alnoor, O. Pilone, O. Nur, M. Willander, *Nanotechnology* **2017**, *28*, 285705.
[55] A. Savoyant, H. Alnoor, S. Bertaina, O. Nur, M. Willander, *Nanotechnology* **2017**, *28*, 035705.
[56] N. Jedrecy, H. J. Von Bardeleben, Y. Zheng, J. L. Cantin, *Phys. Rev. B.* **2004**, *69*, 041308.
[57] P. Lommens, F. Loncke, P. F. Smet, F. Callens, D. Poelman, H. Vrielinck, Z. Hens, *Chem. Mater.* **2007**, *19*, 5576 – 5583.
[58] W. Mader, A. Recnik, *Phys. Status Solidi A* **1998**, *166*, 381 – 395.
[59] C. T. Koch, Ph.D. Thesis, Determination of core structure periodicity and point defect density along dislocations. Phoenix, AZ: Arizona State University; **2002**.
[60] L. P. Bauermann, A. Del Campo, J. Bill, F. Aldinger, *Chem. Mater.* **2006**, *18*, 2016 – 2020.
[61] H. F. Greer, W. Zhou, M. H. Liu, Y. H. Tseng, C. Y. Mou, *CrystEngComm* **2012**, *14*, 1247 – 1255.
[62] S. Hussain, T. M. Liu, M. Kashif, B. Miao, J. J. He, W. Zeng, Y. Zhang, U. Hashim, F. S. Pan, *Mater. Lett.* **2014**, *118*, 165 – 168.
[63] M. L. Fuller, *J. Appl. Phys.* **1944**, *15*, 164 – 170.
[64] X. Liu, X. Wu, H. Cao, R. P. H. Chang, *J. Appl. Phys.* **2004**, *95*, 3141 – 3147.
[65] M. Shiojiri, C. Kaito, *J. Cryst. Growth* **1981**, *52*, 173 – 177.
[66] H. Iwanaga, T. Yoshie, T. Yamaguchi, N. Shibata, *Jap. J. Appl. Phys.* **1983**, *22*, 1098 – 1100.
[67] J. C. Kim, E. Goo, *J. Am. Ceram. Soc.* **1990**, *73*, 877 – 884.
[68] R. X. Bian, L. L. Meng, M. Zhang, L. L. Chen, H. Liu, *ACS Omega* **2019**, *4*, 1816 – 1823.
[69] S. Acharya, J. P. Hill, K. Ariga, *Adv. Mater.* **2009**, *21*, 2959 – 2981.
[70] D. G. Suciu, O. Smigelschi, E. Ruckstei, *AIChE J.* **1967**, *13*, 1120 – 1124.
[71] Z. Burghard, L. Zini, V. Srot, P. Bellina, P. A. Von Aken, J. Bill, *Nano Lett.* **2009**, *9*, 4103 – 4108.
[72] M. Kratzer, O. P. Dimitriev, A. N. Fedoryak, N. M. Osipyonok, P. Balaz, M. Balaz, M. Tesinsky, C. Teichert, *J. Appl. Phys.* **2019**, *125*, 185305.
[73] M. Kratzer, M. Lasnik, S. Röhrig, C. Teichert, M. Deluca, *Sci. Rep.* **2018**, *8*, 422.
[74] D. D'Agostino, C. Di Giorgio, A. Di Trolio, A. Guarino, A. M. Cucolo, A. Vecchione, F. Bobba, *AIP Adv.* **2017**, *7*, 055010.
[75] X. B. Wang, C. Song, D. M. Li, K. W. Geng, F. Zeng, F. Pan, *Appl. Surf. Sci.* **2006**, *253*, 1639 – 1643.
[76] J. Y. Fu, P. Y. Liu, J. Cheng, A. S. Bhalla, R. Guo, *Appl. Phys. Lett.* **2007**, *90*, 212907.
[77] A. Degen, M. Kosec, *J. Eur. Ceram. Soc.* **2000**, *20*, 667 – 673.
[78] X. L. Hu, Y. Masuda, T. Ohji, K. Kato, *Cryst. Growth Des.* **2010**, *10*, 626 – 631.
[79] B. Song, X. Cui, Y. Q. Wang, L. F. Si, Z. X. Kou, W. W. Tian, C. Yi, Y. M. Sun, *Cryst. Growth Des.* **2016**, *16*, 4877 – 4885.
[80] R. Q. Song, A. W. Xu, B. Deng, Q. Li, G. Y. Chen, *Adv. Funct. Mater.* **2007**, *17*, 296 – 306.
[81] J. L. Gunjakar, Y. K. Jo, I. Y. Kim, J. M. Lee, S. B. Patil, J. C. Pyun, S. J. Hwang, *J. Solid State Chem.* **2016**, *240*, 115 – 121.

Manuscript received: October 10, 2019
Revised manuscript received: December 23, 2019
Accepted manuscript online: January 9, 2020
Version of record online: April 28, 2020

